atmosphere

Article

The Influence of an Increase of the Mediterranean Sea Surface Temperature on Two Nocturnal Offshore Rainbands: A Numerical Experiment

Jordi Mazon [1,*] and David Pino [1,2]

[1] Department of Physics, Unversitat Politècnica de Catalunya, BarcelonaTech, 08034 Barcelona, Spain; david.pino@upc.edu
[2] Institute of Space Studies of Catalonia (IEEC–UPC), 08034 Barcelona, Spain
* Correspondence: jordi.mazon@upc.edu; Tel.: +34-934-134-147

Academic Editor: Ricardo Machado Trigo
Received: 15 January 2017; Accepted: 16 March 2017; Published: 18 March 2017

Abstract: Using the Weather Research and Forecasting (WRF) – Advanced Research WRF (ARW) mesoscale model (WRF–ARW), we investigate how two nocturnal offshore rainbands occurring in the Mediterranean basin are modified in a warmer sea surface temperature (SST). After sunset, the thermal difference between land and sea air increases. Driven by drainage winds or land breeze, the inland cold air interacts with the relatively warmer and moister air over the sea. Vertical movement of sea air over the boundary between the two air masses may induce cloud and rain bands offshore. When an increase of SST is prescribed in the WRF simulations, a change in the precipitation pattern is simulated. The numerical experiments show an increase both in the extension and location of the rainbands and in the precipitation rate. These changes, induced by the modified SST, are analyzed by estimating and comparing several parameters such as the location of level of free convection (LFC), Convective Available Potential Energy (CAPE), or the triggering, deceleration and blockage terms of simplified conceptual models.

Keywords: WRF; numerical experiment; sea surface temperature (SST); density currents; nocturnal rainbands

---

1. Introduction

Offshore precipitation cells and bands along the coastline are commonly observed phenomena during the night and early morning in several areas of the tropics [1–4] and in the Mediterranean basin [5–9]. The mechanism that produces this type of precipitation is mainly associated to drainage wind generated by nighttime radiational cooling. From late afternoon, inland air cools faster than the air located at the coastline and over the sea. Consequently, this cooler and denser air begins to flow towards the coast as it descends from mountain ranges and follows rivers and dry streams. When it interacts with the warmer air over the sea, the structure of this relatively cold air mass resembles a coastal front that may enhance vertical movements of the warm and moist sea air. This ascending sea air may condensate, and in some cases precipitation occurs. Figure 1 shows an schematic representation of this phenomenon.

On the boundary between the two air masses, a convergence area forms. Then, the warmer and moister maritime air (at potential temperature θ_w) is forced to move upwards over the cold air (having potential temperature θ_c). When ascending, this warmer air condensates forming stratiform clouds if the air reaches its lifting condensation level (LCL). In some cases, convective clouds will appear if the corresponding level of free convection (LFC) is reached. In both cases the depth of the colder inland air mass (H) plays an important role in helping the wetter and warmer maritime air mass to reach LCL or LFC [10,11]. No clouds will form if $H <$ LCL.

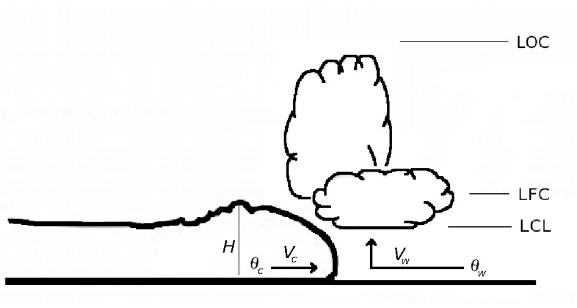

Figure 1. Scheme of cold air (having a deep H, characterized by potential temperature θ_c and drive by wind velocity V_c) flowing offshore and interacting with warmer air over the sea (with potential temperature θ_w and lead by wind velocity V_w). The Lifted Condensation Level is indicated as LCL, the Level of Free Convection as LFC, and the Limit of Convection as LOC.

The location of the clouds and precipitation will depend on the velocity of both air masses (warm, V_w and cold, V_c). For simplification, we assume that the air masses are moving in parallel, opposite directions.

Authors of [10,12,13] showed that the intensity of the synoptic wind (V_w) and the land–sea temperature difference determine the position and the rate of the precipitation. Specifically, V_c increases with the potential temperature difference between the cold and warm air masses. Consequently, if a large land–sea temperature difference exists, the precipitation moves offshore, while large values of V_w move it onshore [14]. As expected, V_c is also influenced by roughness length over land [15].

1.1. Theoretical Parameters

Orography is a common factor that contributes to heavy precipitation events when an unstable flow interacts with mountain ranges [16]. In order to simplify the complexity associated with mountain precipitation, using 3D simulations, authors of [11] defined some parameters to explain the intensity and the location of convective rainfall over an idealized mountain range. For instance, for convectively unstable flows, they define the triggering convection parameter h/LFC, where h is the mountain height. Values greater than 1 of this parameter suggest that convective cells appear over the mountain, while smaller values indicate that convection is inhibited. Another proposed parameter that measures deceleration induced on the upstream flow in low-CAPE conditions is $N\text{LFC}/U$, where N is the the Brunt-Väisälä frequency and U is the horizontal wind speed of the flow blowing perpendicular to the mountain. Finally, for stable flows [17] defined the parameter Nh/U and found that the air flows easily over the mountain ridge with little blockage and minor accelerations on the lee side of the ridge for $Nh/U \approx 0.25$. For $Nh/U \approx 5$, the flow is entirely blocked by the mountain and the air is forced upwards with large vertical accelerations. Moreover, Wang et al. [1] predicted, from modeling studies, that cloud bands would form at the flow separation line between warm and cold air masses if the ratio $B = U/N > \text{LFC}$.

As a first approach, it can be assumed that the cool pool associated with a density current acts as a mountain range that blocks, lifts and decelerates the prevailing warmer flow. Since these two air masses have different densities they do not mix, and consequently the maritime air mass is lifted mainly over the cold one. Thus, the triggering parameter h/LFC (proposed and defined by authors of [11]) can be rewritten as H/LFC. While h and LFC defined in [11] are related to a single air mass, it is important to note that in our case H is related to the height of the cool pool while LFC is calculated over a warmer and moister maritime air mass. In the same way, the blockage parameter defined in [17] is redefined as NH/U, where U is the relative wind speed of the two air masses. The Brunt-Väisälä frequency, N is evaluated near the boundary between cold and warm air masses, quantifying the stability of the environment. It is evaluated according to the expression:

$$N = \sqrt{\frac{d\theta}{dz}\frac{g}{\theta}}, \tag{1}$$

Here, $d\theta/dz$, is the vertical gradient of potential temperature (θ) with height (z). Although these theoretical parameters do not take into account the synoptic features and consider only idealized profiles, they have already been used to describe some coastal precipitation events in the Mediterranean basin by authors of [9].

1.2. SST on the Mediterranean Basin

Sea surface temperature (SST) and air temperature control moisture and heat fluxes over the sea. According to [18], when a front is formed, the depth of the cold air mass (H) is directly proportional to the virtual potential temperature of the warm air mass, in our case the maritime air mass. In particular, the higher the temperature and moisture of sea air (influenced by SST), the higher the sea air virtual potential temperature. Consequently, H can grow helping the maritime air to reach LFC. In a previous work, [15] concluded, by using mesoscale numerical experiments, that increasing SST enhances rainfall rates over the sea. In [19] it was shown that an increase in SST affects the intensity and the characteristics of tropical-like cyclones in the Mediterranean. Additionally, by performing numerical experiments in [20], the sensibility of modeled precipitation with the SST over the Mediterranean was shown, founding an increase of the precipitation rate and extension but moved offshore.

According to the Fourth and Fifth Assessment Report from the Intergovernamental Panel on Climate Change (IPCC, [21]), the SST worldwide has increased by an average of 0.7 °C from the beginning of the 20th century [22]. Particularly, in the west Mediterranean basin SST has increased by approximately 0.6 °C [23,24]. This value is consistent with the regular measurements of SST 4 km offshore of the northeast coast of the Iberian Peninsula, where a clear increase in SST of around 0.7 °C has been recorded over the last 30 years [25,26].

Moreover, at the end of the 21st Century, a large increase in SST over the whole Mediterranean basin has been projected for all seasons with the Sea Atmosphere Mediterranean Model (SAAM) [27]. The increase in SST in the whole Mediterranean basin in the IPCC–A2 scenario was evaluated by performing several SAAM numerical experiments over the period 1960–2099. SST anomalies found for the 30-year average in the period 2070–2099 compared to the 1961–1990 control period are: between 2.5 and 3 °C in the western Mediterranean region in summer (near the Iberian Peninsula coastline); and between 2 and 2.5 °C in the eastern Mediterranean region during winter [28].

The relationship between SST and CAPE has been studied by several authors. According to [29], over the tropical Pacific area, with an increase of 2 °C the SST enhances the local evaporation and CAPE increases by 800 $\mathrm{J \cdot kg^{-1}}$. These authors show that the air temperature lapse rate hardly changes and has little contribution to CAPE variation. Authors of [30] investigated the response of CAPE to a warm SST over the Pacific by using global circulation models. According to these authors, CAPE would increase of around 200 $\mathrm{J \cdot kg^{-1}}$ in most regions over the Pacific ocean if SST increases 2 K. Regarding convective clouds intensity, according to authors of [30], an increase of CAPE around 200 $\mathrm{J \cdot kg^{-1}}$ would result in a 10%–15% increase in the updraft air parcel velocity. These authors also show that, as a consequence of the increase of 2 K in SST, an increase of 4 $\mathrm{m \cdot s^{-1}}$ in the cumulus updraft velocity is estimated.

Here we investigate how offshore rainbands in the Mediterranean basin may be modified by an increase of SST in the area based on IPCC projections. We select the two episodes producing the heaviest precipitation in the Mediterranean basin among the 10 studied by authors of [9] and we analyze how the location and intensity of the precipitation is modified when the projected SST increase is included in the simulations. We study the rainband (RB) which occurred on 6 January 6 2011 in the eastern part of the basin (near the Israeli coast, RB1), and the rainband that occurred on 6 September

6 2011 in the western Mediterranean basin (at the northeast of the Iberian Peninsula, hereafter RB2). Figure 2 shows the location of these RBs in the Mediterranean basin.

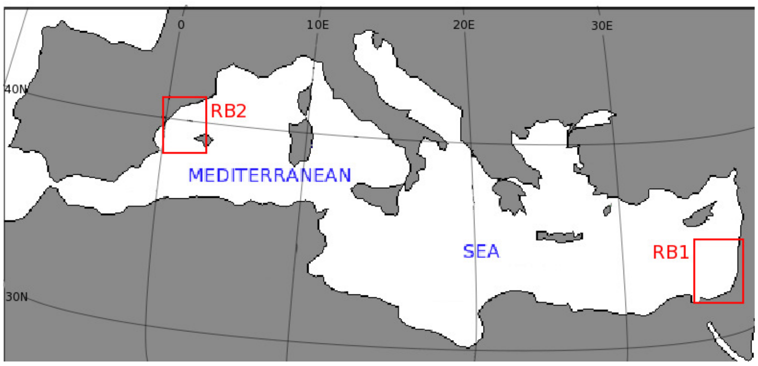

Figure 2. The Mediterranean basin. The squares mark the location where the influence of surface sea temperature (SST) on two coastal rainbands are analyzed.

The structure of the paper is as follows. In Section 2 the methodology is described. Sections 3 and 4 are dedicated to showing and describing the simulations for the control run (CR) and for the simulations where SST is increased (SSTR) for each studied case, respectively. The paper ends with the main conclusions.

2. Methodology

The two selected rainbands, RB1 and RB2 produced the heaviest precipitations among the ones studied in [9]. These authors focused their analysis in describing the mechanism driving the formation of these RB by using radar and satellite imagery and mesoscale numerical simulations.

Here by using the same mesoscale model, the WRF–ARW [31], we perform additional simulations (SSTR) where the SST is modified in the European Center Medium Weather Forecasting (ECMWF) data following the results of [27] in the different parts of the Mediterranean basin in the corresponding season: a 2.2 K increase of SST for the RB1 (occurred during winter at the eastern Mediterranean) and 2.5 K for the RB2 (which occurred at the end of summer, in the western part of the Mediterranean basin).

It is important to note that the aim of this investigation is not to evaluate the influence of global warming in precipitation produced by the mechanism described above, but to analyze the influence of these coastal rainbands in the Mediterranean basin on an increase of SST.

The variables used in the analysis (the comparison between CR and SSTR results) are: the 10-h accumulated precipitation, wind field, depth of the cold air mass and the estimated parameters that account for the triggering, blockage and deceleration that the cold air mass offers to the prevailing maritime air [1,11,17].

WRF Set-Up

Version 3.3 of the WRF–ARW model is used to simulate the atmospheric dynamics during the two episodes. The domains defined to simulate both precipitation episodes are shown in Figure 3. The left panel shows the four nested domains defined for the episode occuring in the eastern Mediterranean basin on 6 January 6 2011, with horizontal grid spaces of 27, 9, 3 and 1 km, and 50 × 40, 76 × 64, 85 × 97 and 70 × 70 points, respectively. The simulation begins at 00:00 on 5 January, and finishes at 18:00 UTC on 7 January, 2011. The right panel in Figure 3 shows the three nested domains defined for the episode occurring on 6 September 6 2011 in the western part of the Mediterranean basin, with a horizontal grid space of 18, 6 and 2 km, and 80 × 80, 121 × 112 and

148 × 148 points, respectively. The simulation begins at 00:00 on 5 September, 2011 and finishes at 18:00 UTC on 7 September, 2011.

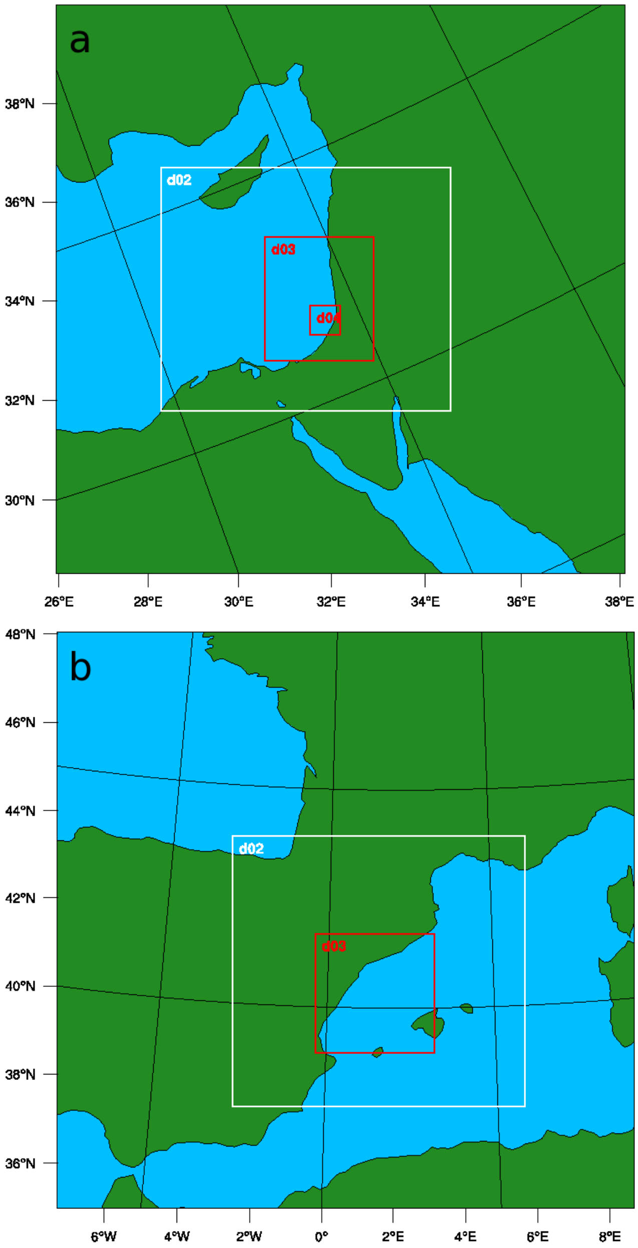

Figure 3. Domains defined in the WRF simulations. The panel (**a**) shows the domains for the episode occurring on 6 January, 2011 in the eastern Mediterranean basin (RB1). Panel (**b**) shows the domains for the episode occurring in the western basin on 5 September, 2011 (RB2).

In all the simulations 42 η–vertical levels have been defined, 23 levels below 1 km. With respect to the physical parameterizations, the MRF [32] scheme is used for the PBL, and RRTM scheme for longwave radiation [33]; the MM5 shortwave scheme for shortwave radiation [34]; and WSM 6–class scheme [35] for the microphysics parameterization. No cumulus parameterization is used for any of the smallest domains because its horizontal resolution is lower than 3 km in all the simulations. In the larger domains the Kain–Fritsch Scheme is used [36].

The initial and boundary conditions were updated every six hours with information obtained from the reanalysis of the ECMWF model at 0.125° of horizontal resolution. In all the simulations performed two-way nested domains have been used.

3. The Rainband in the Eastern Mediteranean Basin: RB1

3.1. Observations

According to the 3-h accumulated precipitation detected by Tropical Rainfall Measurement Mission (TRMM) [37], the precipitation appeared after 21:00 UTC on 5 January, and disappeared before 06:00 UTC on 6 January 2011. Figure 4a shows the 3-h accumulated precipitation at 03:00 UTC obtained by the TRMM satellite with a maximum value of around 18 mm off the southern coastline of Israel, and lower values at the northern coastline, from 4 to 8 mm. Figure 4b shows the Meteosat satellite infrared image at 03:00 UTC on January 6, 2011, where an offshore cloud band is observed in front of the Israel coastline at 03:00 UTC.

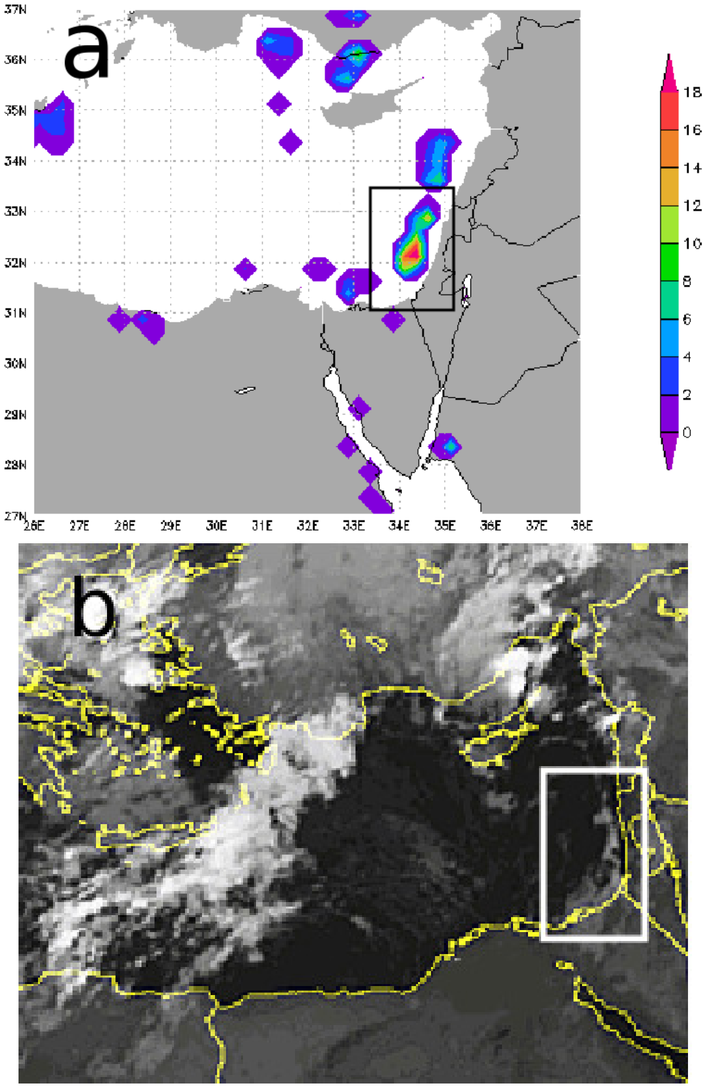

Figure 4. (**a**) 3-h accumulated precipitation estimated by TRMM at 03:00 UTC on 6 January 2011 and (**b**) Infrared (IR) Meteosat satellite image at 03:00 UTC on 6 January 2011. The square indicates the location of domain 3 used in the simulation.

3.2. Numerical Simulations

Figure 5 shows the simulated 10-h accumulated precipitation in the smallest domain at 08:00 UTC on 6 January 2011, obtained by (a) CR and (b) SSTR numerical simulations. Both lines of precipitation are formed by several precipitations cells, with maximum values of 10-h accumulated precipitation around 26 mm in both cases. However, the precipitation simulated by CR is closer to the coast. Moreover, in the SSTR simulation the precipitation area is wider and a large number of cells show higher values of 10-h accumulated precipitation.

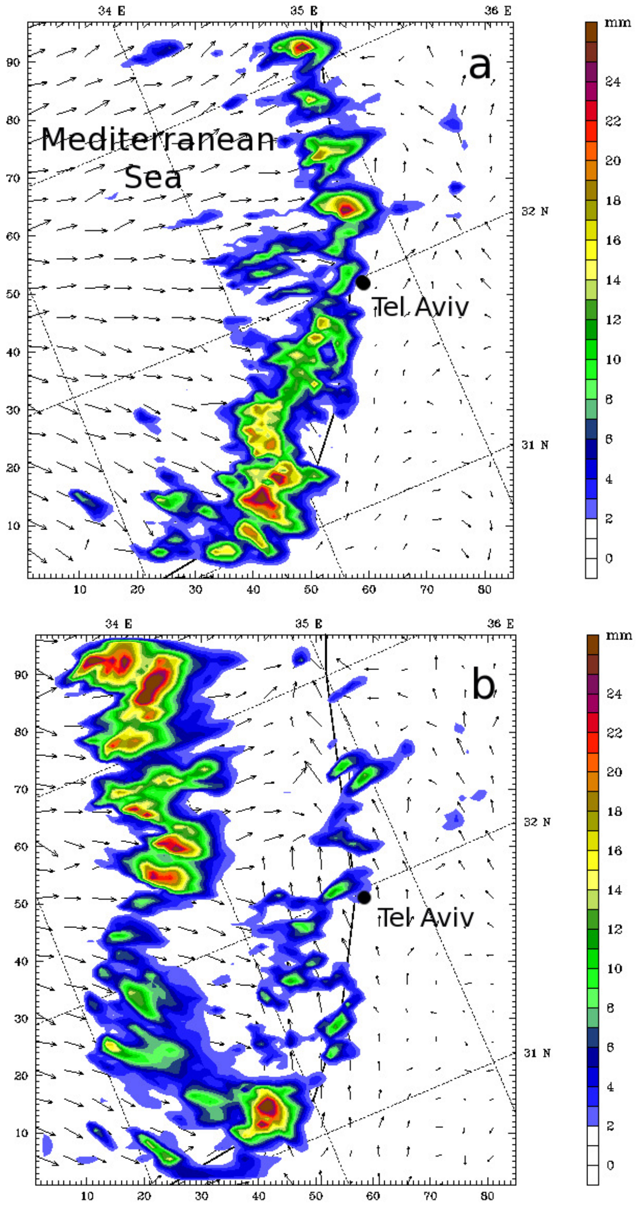

Figure 5. Simulated 10-h accumulated precipitation (color contours) and surface wind field (arrows) at the smallest domain on 6 January 2011 at 08:00 UTC, obtained by (**a**) CR and (**b**) SSTR (ΔSST=2.2 K).

The differences in the location of the precipitation between the two numerical experiments can be explained because greater land–sea air temperature difference increases thermal wind velocity i.e., the speed of the colder air mass [38]. Consequently, for the SSTR numerical simulation the line of precipitation is shifted several kilometers offshore and the precipitation occurs mainly over the sea, while inland areas received less precipitation. Figure 6 shows the wind speed difference between CR and SSTR numerical simulation at 04:00 UTC. Warm colors indicate an increase in wind speed for SSTR. Higher SST increases the drainage wind speed by 5 m·s^{-1} in some areas. Consequently, the stronger wind moves the line of precipitation offshore with respect to CR simulation.

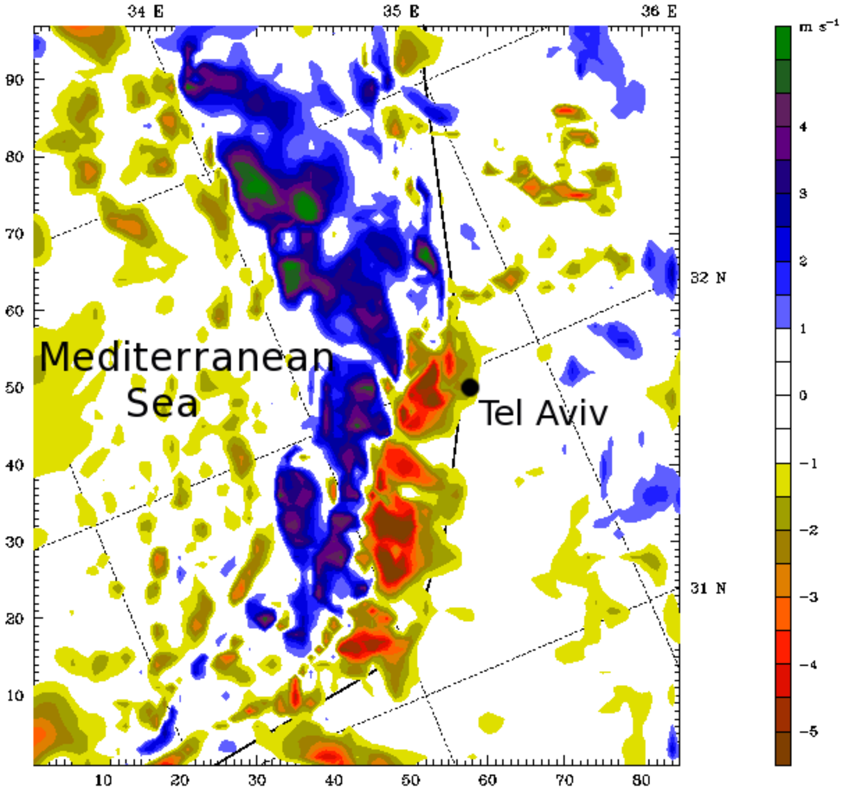

Figure 6. Simulated surface wind speed difference between CR and SSTR at 04:00 UTC on January 6, 2011 in the smallest domain. Negative values (warm colors) indicate intensification of the wind velocity for SSTR.

Regarding the cold air depth, some significant differences between CR and SSTR are noticed. Lower values of H are obtained in SSTR numerical experiment, especially from 04:00 UTC. For instance, at 06:00 UTC H is around 1000 m height in CR, while H is around 700 m height in SSTR (not shown).

Figure 7 shows the temporal evolution of the parameters that account for the triggering, blockage and deceleration that the cold air offers to the prevailing flow from 00:00 to 09:00 UTC for SSTR (dashed lines) and CR simulations (solid lines). These parameters are evaluated over the cold air depth as described in [11] in idealized mountains and applied by [9] over some coastal fronts, from the variables obtained by WRF simulation.

Regarding the triggering term (H/LFC), lower values are estimated in the SSTR with respect to CR but they are not due to differences in LFC. No significant variations are noticed from 00:00 to 09:00 UTC, LFC is located approximately at the same height in both simulations. The reduction in the estimated values of the triggering parameter is due to a lower estimation of H in SSTR. Despite the lower triggering term, higher precipitation rates are simulated along the rainband in SSTR, and the precipitation is wider. This can be explained because the triggering term does not take into account the vertical wind speed of the ascending air, only accounting for the relation between the cold air mass height, H, with respect to the LFC (note that H remains always around 1). The simulated vertical velocity at the head of the cold air mass is higher in SSTR, and consequently, larger amount of heat and humidity in a warmer SST can reach higher atmospheric levels. Consequently, thicker clouds can be formed.

Focusing on the blockage term (NH/U), lower values are estimated for SSTR, which is consistent with the fact that H is lower in the SSRT. Furthermore, the upward maritime flow has a lower deceleration ($N\mathrm{LFC}/U$). Therefore, the maritime wet air can reach higher levels with respect to the CR, forming deeper clouds, which produce a larger amount of precipitation, as shown in Figure 5b. Moreover, SSTR simulates slightly higher values of CAPE, reaching a maximum value of 962 $\mathrm{J{\cdot}kg^{-1}}$ over the cold air mass head at 06:00 UTC, whereas the maximum value of CAPE in CR is 871 $\mathrm{J{\cdot}kg^{-1}}$.

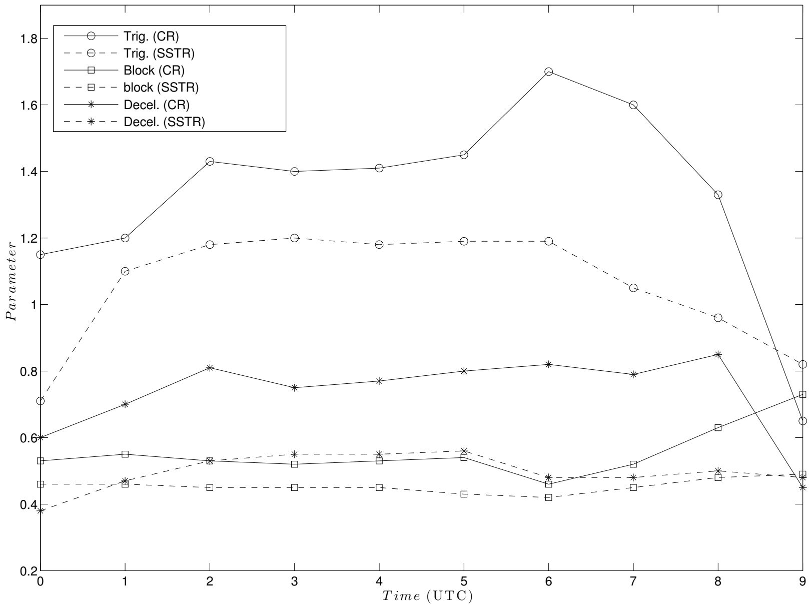

Figure 7. Temporal evolution on 6 January 2011 of the estimated triggering, H/LFC (circles), blockage, NH/U (asterisks) and deceleration, $N\mathrm{LFC}/U$ (squares) parameters in the SSTR simulation (dashed lines) and the CR (closed lines) simulations.

4. The Rainband in the Western Mediterranean Basin: RB2

4.1. Observations

The reflectivity radar images show a rainband at the northeast of the Iberian Peninsula from 22:00 UTC from 5 September 2011 to the early morning on 6 September 2011 (see Figure 8a). Several weak and isolate precipitation cells located parallel to the coastline were observed. Figure 8b shows these cells forming a line of precipitation on 6 September 2011 at 01:00 UTC. Figure 8c,d shows the rainband moving offshore from 03:00 until 08:00 UTC. This line of precipitation had an extension around of 150–200 km from 05:00 to 07:00 UTC on 6 September 2011.

Clouds associated to this rainband were also recorded by satellite sensing. Figure 9a shows the thermal channel image recorded by Meteosat at 03:00 UTC, where clouds can be observed over the same area in which reflectivity radar recorded precipitation. Finally, Figure 9b shows the 3-h accumulated precipitation estimated at 03:00 by TRMM, at approximately the same location in where the meteorological radar and Meteosat satellite recorded precipitation and clouds.

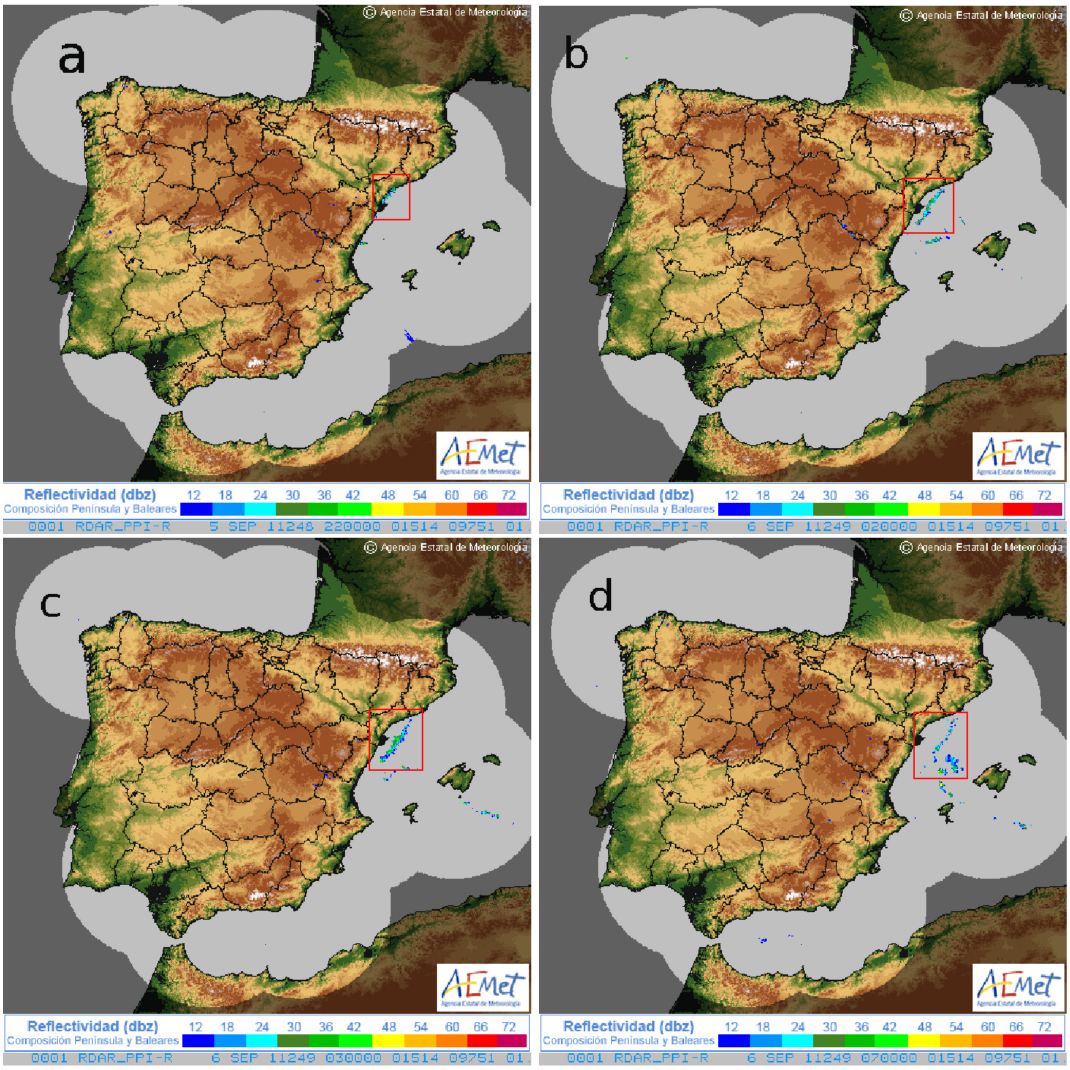

Figure 8. Reflectivity radar images recorded by the Spanish Weather Agency (AEMET) radar network on 4 September 2011 at (**a**) 22:00 UTC , and on 5 September 2011 at (**b**) 01:00 UTC, (**c**) 03:00 UTC and (**d**) 08:00 UTC. The red square indicates the location of the rainband associated with the coastal fronts analyzed in this section.

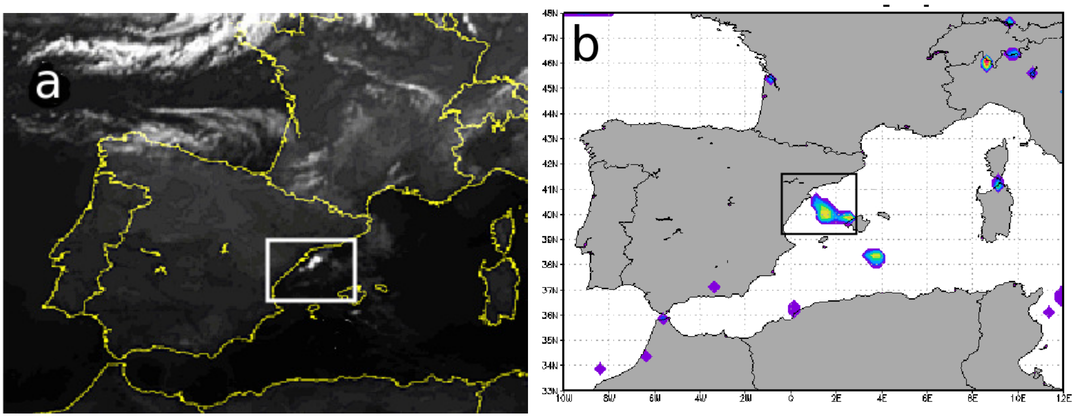

Figure 9. (**a**) Thermal IR channel of the Meteosat satellite and (**b**) the 3-h accumulated precipitation estimated by TRMM on 6 September 2011 at 03:00 UTC. The square indicates the location of domain 3 used in the corresponding simulation.

4.2. Numerical Simulations

Figure 10 shows the simulated 10–h accumulated precipitation at 08:00 UTC on 6 September 2011 obtained by (a) CR and (b) SSTR. CR shows a rainband of accumulated precipitation near and approximately parallel to the coastline, that reaches around 30 mm over 10 h in several areas. In SSTR the 10–h accumulated precipitation shows higher values in many parts of the rainband. Additionally, in SSTR the rainband moves away from the coast and is no longer parallel to the coastline. (see Figure 10b).

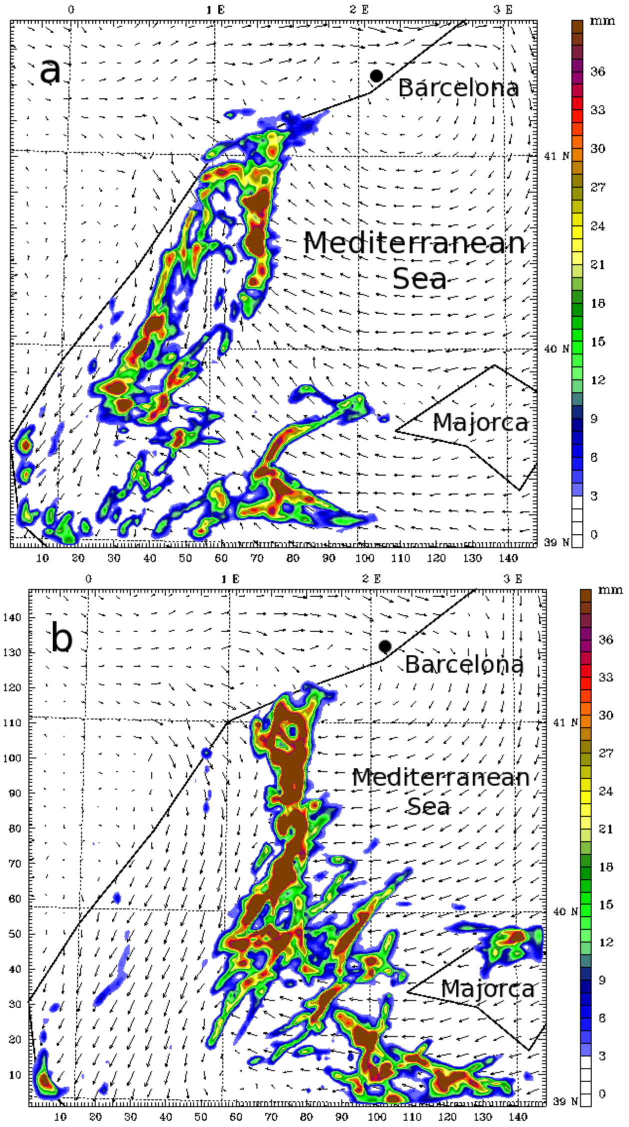

Figure 10. Simulated 10-h accumulated precipitation (color contours) and surface wind field (arrows) in the smallest domain at 08:00 UTC on 6 September 2011, simulated by (**a**) CR and (**b**) SSTR (ΔSST = 2.5 K).

In order to explain these features, Figure 11 shows the wind speed difference on 6 September 2011 at 01:00 UTC between CR and SSTR. Negative values indicate that the velocity is higher in SSTR. The intensified velocity of the drainage winds is noted by observing the red colors near the coastline. This suggests that the inland cold air moves offshore faster as a consequence of the higher velocity of the drainage winds, due to the larger temperature difference between land and sea air masses in SSTR. It is remarkable that at the northern extreme of the rainband weak differences in wind velocity are simulated close the coastline. The precipitation here slightly moves offshore, while the center and southern part of the rainband move faster offshore lead by the increased drainage winds.

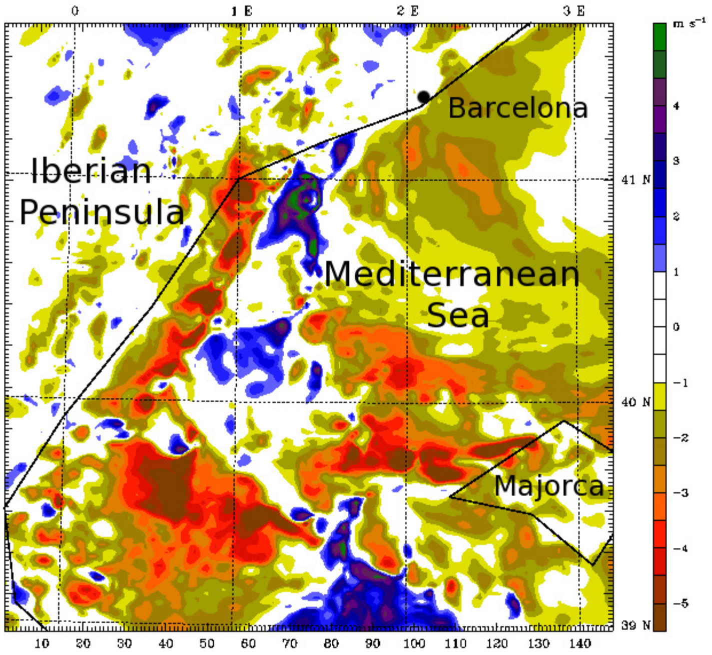

Figure 11. Simulated wind speed difference between CR and SSTR in the smallest domain on 6 September 2011 at 01:00 UTC. Negative values (warm colors) indicate intensification of the wind velocity for SSTR.

Figure 12 shows the temporal evolution of the parameters that account for the triggering, blockage and deceleration that the cold air offers to the prevailing flow from 00:00 to 09:00 UTC on 6 September 2011 estimated in the SSTR (dashed lines) and CR (solid lines) simulations.

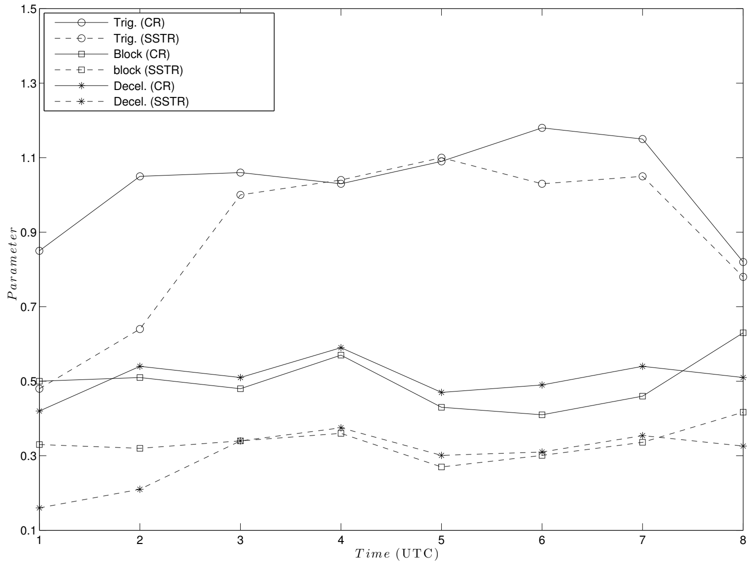

Figure 12. Temporal evolution on 6 September 2011 of the triggering, H/LFC (circles), blockage, NH/U (asterisks) and deceleration, $N\mathrm{LFC}/U$ (squares) parameters in the SSTR simulation (dashed lines) and the CR (lines) simulations.

Regarding the triggering term, lower values are estimated in SSTR between 00:00 and 03:00, and quite similar values from 03:00 to 09:00 UTC. This can be explained because LFC shows quite similar values in both simulations, while H shows slight lower values in SSTR from 00:00 to 03:00 UTC, and similar values for the rest of the night.

With respect to the blockage and deceleration terms, quite similar values are estimated in both simulations, suggesting that the air flows in a similar way around the cold air mass.

Furthermore, simulated CAPE is larger in SSTR, reaching maximum values around 1700–1800 $\mathrm{J\cdot kg^{-1}}$ (where maximum 1400–1600 $\mathrm{J\cdot kg^{-1}}$ in CR).

5. Conclusions

The influence of an SST increase on the precipitation associated to two cases of interactions of warm–cold air masses in the Mediterranean basin has been performed by using WRF simulations. These experiments consist of increasing the SST by 2.2 and 2.5 K, depending on the studied episode, according the projections obtained by [27] based on IPCC projections.

In the simulations with increasing SST, the precipitation associated to the rainbands shifted offshore on comparison with the CR simulations. Moreover, wider precipitation areas, with higher amounts of accumulated precipitation, are simulated in SSTR.

Concerning the wind, SSTR simulations show that drainage wind speed increases close to the coastline. In these numerical simulations, the warmer sea-air induced by higher SST enhances the speed of drainage winds, which moves further offshore than in the CR simulation.

Simulated values of CAPE over the boundary between the two air masses are also larger for SSTR: an increase of 200–300 $\mathrm{J\cdot kg^{-1}}$ in RB2, and near 100 $\mathrm{J\cdot kg^{-1}}$ in RB1. These values are lower than those obtained in [29], where it was found that over the tropical Pacific area an increase of 2 K in the SST implies at least an increase of 800 $\mathrm{J\cdot Kg^{-1}}$ in CAPE. However, the modification of the simulated CAPE is in a good agreement with that obtained by [30]. These authors found that CAPE increases around 200 $\mathrm{J\cdot kg^{-1}}$ over the Pacific ocean if SST increases 2 K. According to these authors, an increase of CAPE of 200 $\mathrm{J\cdot kg^{-1}}$ would result in a 10–15% increase in updraft air parcel velocity, of around 4 $\mathrm{m\cdot s^{-1}}$.

The modifications to the triggering, the blockage and the deceleration that the cold air offers to the prevailing maritime sea–air have been also analyzed. Concerning the triggering term, lower values are estimated in the SSTR with respect to the CR, due to lower values of the estimated cold air mass depth, H, in SSTR. The blockage parameter shows lower values in the SSTR with respect to CR, which is consistent with the fact that H shows lower values in the SSRT. Furthermore, as H decreases in the SSTR, the upward maritime flow has a lower deceleration, as the estimated deceleration term has shown.

Although global warming has many and complex interactions with atmospheric dynamics, the variation of SST is a key factor that influences coastal precipitation. As has been shown, in a warmer Mediterranean sea the rainbands are simulated further offshore, associated with higher amounts of precipitation which fall over the sea. This may affect some regions where this type of precipitation is a significant source of water.

Acknowledgments: The numerical simulations were performed by using the resources of the Supercomputing Center of Catalonia (CSUC). The authors were partially financed by the Spanish MINECO project CGL2016–75996–R. The images and data used in this study were acquired using the GES-DISC Interactive Online Visualization And Analysis Infrastructure (Giovanni) as part of NASA's Goddard Earth Sciences (GES) Data and Information Services Center (DISC). The authors are also grateful to the Spanish Weather Agency (AEMET) for allowing the use of reflectivity images, as well as to EUMETSAT for the Meteosat images.

Author Contributions: Jordi Mazon conceived the idea, designed and performed the numerical simulations, and wrote the paper. David Pino provided the data for the simulations and contributed to analyse the results as well as to write the paper.

Conflicts of Interest: The authors declare no conflict of interest.

References

1. Wang, J.J.; Rauber, R.; Ochs, H.T.I.; Carbone, R.E. The effects of the island of Hawaii on offshore rainband evolution. *Mon. Weather Rev.* **2000**, *128*, 1052–1069.
2. Ohsawa, T.; Ueda, H.; Hayashi, T.; Watanabe, A.; Masumoto, J. Diurnal variations of convective activity and rainfall in tropical Asia. *J. Meteorol. Soc. Jpn.* **2003**, *79*, 333–352.
3. Mapes, B.; Warner, T.; Xu, M.; Negri, A. Diurnal patterns of rainfall in northwestern South America. Part III: Diurnal gravity waves and nocturnal convection offshore. *Mon. Weather Rev.* **2003**, *131*, 830–884.
4. Yu, C.K.; Jou, B.J. Radar observations of the diurnal forced offshore convection lines among the southeastern coast of Taiwan. *Mon. Weather Rev.* **2004**, *133*, 1613–1636.
5. Neumann, J. Land breezes and nocturnal thunderstorms. *J. Meteorol.* **1951**, *8*, 60–67.
6. Greich, Y.; Mozes, H.; Rosenfeld, D. Radar analysis of cloud systems and their rainfall yield in Israel. *Isr. J. Earth Sci.* **2004**, *53*, 63–76.
7. Mazon, J.; Pino, D. The role of nocturnal Low–Level–Jet in nocturnal convection and rainfalls in the west Mediterranean coast: The episode of 14 December 2010 in northeast of Iberian Peninsula. *Adv. Sci. Res.* **2011**, *8*, 27–31.
8. Mazon, J.; Pino, D. Numerical simulation of relatively heavy nocturnal rainbands associated with nocturnal coastal fronts in the Mediterranean basin. *Nat. Hazards Earth Syst. Sci. Discuss* **2013**, *1*, 7595–7613.
9. Mazon, J.; Pino, D. Role of the nocturnal coastal–front depth on cloud formation and precipitacion in the Mediterranean basin. *Atmos. Res.* **2015**, *153*, 145–154.
10. Schoenberg, L.M. Doppler radar observation of land–breeze cold front. *Geophys. Res. Lett.* **1984**, *112*, 2455–2464.
11. Miglietta, M.; Rotunno, R. Numerical simulations of low–CAPE flows over a mountain ridge. *J. Atmos. Sci.* **2010**, *67*, 2391–2401.
12. Meyer, J.H. Radar observations of land breeze fronts. *J. Appl. Meteorol.* **1971**, *10*, 1224–1232.
13. Heiblum, R.H.; Koren, I.; Altaratz, O. Coastal precipitation formation and discharge based on TRMM observations. *Atmos. Chem. Phys.* **2011**, *11*, 13201–13217.
14. Mapes, B.; Warner, T.; Xu, M.; Negri, A. Diurnal patterns of rainfall in northwestern South America. Part I: Observations and context. *Mon. Weather Rev.* **2003**, *131*, 799–812.
15. Malda, D.; Vilà-Guerau de Arellano, J.; van der Berg, W.D.; Zuurendonk, I.W. The role of atmospheric boundary layer-surface interactions on the development of coastal fronts. *Ann. Geophys.* **2007**, *25*, 341–360.
16. Lin, Y.L.; Chiao, S.; Wang, T.A.; Kaplan, M.; Weglarz, R. Some common ingredients for heavy orographic rainfall. *Weather Forecast.* **2001**, *16*, 633–660.
17. Durran, D.R.; Klemp, J.B. Another look at down–slope winds. Part II: Nonlinear amplification beneath wave–overturning layers. *J. Atmos. Sci.* **1987**, *44*, 3402–3412.
18. Simpson, J.E.; Britter, R.E. A laboratory model of atmospheric mesofront. *Q. J. R. Meteorol. Soc.* **1980**, *106*, 485–500.
19. Miglietta, M.; Moscatello, A.; Conte, D.; Mannarini, G.; Lacarata, G.; Rotunno, R. Numerical analysis of a Mediterranean hurricane over south-eastern Italy: Sensitivity experiments to sea surface temperature. *Atmos. Res.* **2011**, *101*, 412–426.
20. Senatore, A.; Mendicino, G.; Knoche, H.-R.; Kunstmann, H. Sensitivity of modeled precipitation to sea surface temperature in regions with complex topography and coastlines: A case study for the Mediterranean. *J. Hydrometeorol.* **2014**, *15*, 2370–2396.
21. Kavvada, A.; Ruiz-Barradas, A.; Nigam, S. *Climate Change 2013: The Physical Science Basis. Contribution of Working Group I to the Fifth Assessmant Report of the Interguvernamental Panel on Climate Change*; Technical Report; Cambrige University Press: Cambrige, UK, 2013.
22. Trenberth, K.E.; Jones, P.H.; Ambenje, P.; Bojariu, R.; Easterling, D.; Tank, A.K.; Parker, D.; Rahimzadeh, F.; Renwick, J.A.; Rusticucci, M.; et al. *Climate Change 2007: The Physical Science Basis. Contribution of Working Group I to the Fourth Assessment Report of the Intergovernmental Panel on Climate Change*; Chapter 3. Observations: Surface and Atmospheric Climate Change; Solomon, S., Qin, D., Manning, M., Chen, Z., Marquis, M., Averyt, K.B., Tignor, M., Miller, H.L., Eds.; Cambridge University Press: Cambridge, UK, 2007.

23. Rixen, M.; Beckers, J.; Levitus, S.; Antonov, J.; Boyer, T.; Maillard, C.; Fichaut, M.; Balopoulos, E.; Iona, S.; Dooley, H.; et al. The Western Mediterranean deep water: A proxy for climate change. *Geophys. Res. Lett.* **2005**, *32*, doi:10.1029/2005GL022702.
24. Vargas-Yáñez, M.; García, M.J.; Salat, J.; García-Martínez, M.C.; Pascual, J.; Moya, F. Warming trends and decadal variability in the Western Mediterranean shelf. *Glob. Planet. Chang.* **2008**, *63*, 177–184.
25. Salat, J.; Pascual, J. The oceanographic and meteorological station at l'Estartit (NW Mediterranean). In *Tracking Long-Term Hydrographical Change in the Mediterranean Sea*; CIESM Workshop Series; CIESM: Madrid, Spain, 2002; pp. 29–32.
26. Salat, J.; Pascual, J. *Principales Tendencias Climatológicas en el Mediterráneo Noroccidental, a Partir de más de 30 años de Observaciones Oceanográficas en la Costa Catalana*; Clima, Sociedad y Medio Ambiente. Asociación Española de Climatología: Madrid, Spain, 2006; Volume Serie A, pp. 284–290.
27. Somot, S.; Sevault, F.; Déqué, M.; Crépon, M. 21st century climate change scenario for the Mediterranean using a coupled atmosphere–ocean regional climate model. *Glob. Planet. Chang.* **2008**, *63*, 112–126.
28. Kavvada, A.; Ruiz-Barradas, A.; Nigam, S. AMOs structure and climate footprint in observations and IPCC AR5 climate simulations. *Clim. Dyn.* **2013**, *41*, 1345–1364.
29. Williams, E. Global circuit response to seasonal variations in global surface air temperature. *Mon. Weather Rev.* **1994**, *117*, 1917–1929.
30. Ye, B.; del Genio, A.; Lo, K.K.W. CAPE variations in the current climate and in a climate change. *J. Clim.* **1998**, *11*, 2985–3002.
31. Skamarock, W.C.; Klemp, J.B.; Dudhia, J.; Gill, D.O.; Barker, D.M.; Duda, M.; Huang, X.Y.; Wan, W.; Powers, J.G. *A Description of the Advanced Research WRF Version 3*; Technical Report TN–475+STR; NCAR: Boulder, CO, USA, 2008.
32. Hong, S.Y.; Pan, H.L. Nonlocal boundary layer vertical diffusion in a medium-range forecast model. *Mon. Weather Rev.* **1996**, *124*, 2322–2339.
33. Mlawer, E.J.; Taubman, S.J.; Brown, P.D.; Iacono, M.J.; Clough, S.A. Radiative transfer for inhomogeneous atmospheres: RRTM, a validated correlated–k model for the longwave. *J. Geophys. Res.* **1997**, *102*, 663–682.
34. Dudhia, J. Numerical study of convection observed during the winter monsoon experiment using a mesoscale two–dimensional model. *J. Atmos. Sci.* **1989**, *46*, 3077–3107.
35. Hong, S.H.; Dudhia, J.; Chen, S.H. A revised approach to ice microphysical processes for the bulk parameterization of clouds and precipitation. *Mon. Weather Rev.* **2004**, *132*, 103–120.
36. Kain, J. The Kain–Fritsch convective parameterization: An update. *J. Appl. Meteorol.* **2004**, *43*, 170–181.
37. Haddad, Z.S.; Smith, E.A.; Kummerow, C.D.; Iguchi, T.; Farrar, M.R.; Durnen, S.L.; Alves, M.; Olson, W.S. The TRMM 'day–1' radar/radiometer combined rain profiling algorithm. *J. Meteorol. Soc. Jpn.* **1997**, *75*, 799–809.
38. Khain, A.P.; Rosenfeld, D.; Sednev, I.L. Coastal effects in the Eastern Mediterranean as seen from experiments using a cloud ensemble model with a detailed description of warm and ice microphysical processes. *Atmos. Res.* **1993**, *30*, 295–319.